Journal of Energy Storage 55 (2022) 105558

Contents lists available at ScienceDirect

Journal of Energy Storage

journal homepage: www.elsevier.com/locate/est

Research papers

Li-ion battery degradation modes diagnosis via Convolutional Neural Networks

N. Costa [a,*], L. Sánchez [a], D. Anseán [b], M. Dubarry [c]

[a] Computer Science Department, Polytechnic School of Engineering, University of Oviedo, Gijon, 33202, Asturias, Spain
[b] Department of Electrical Engineering, Polytechnic School of Engineering, University of Oviedo, Gijon, 33204, Asturias, Spain
[c] Hawaii Natural Energy Institute, SOEST, University of Hawaii at Manoa, 1680 East-West Road, Honolulu, POST 109, HI 96822, USA

ARTICLE INFO

Dataset link: http://dx.doi.org/10.17632/bs2j56pn7y.3, http://dx.doi.org/10.17632/6s6ph9n8zg.3, http://dx.doi.org/10.17632/2h8cpszy26.1, http://dx.doi.org/10.17632/pb5xpv8z5r.1

Keywords:
Battery diagnosis
Degradation modes
Deep learning
Convolutional Neural Networks

ABSTRACT

Lithium-ion batteries are ubiquitous in modern society with a presence in storage systems, electric cars, portable electronics, and many more applications. Consequently, to enable safe and reliable use of LIB systems, diagnosis and prognosis have become critical. Within the field of Artificial Intelligence, Deep Learning algorithms have achieved significant impacts for image or object recognition, yet their application for battery diagnosis is still at an early developing stage. In this paper, we propose a novel approach for battery degradation diagnosis based on the representation of battery data as images, in order to leverage the use of well-established Convolutional Neural Networks. Accuracy for diagnosis, via the quantification of degradation modes was tested on synthetic data. Our approach was shown to be more accurate than current methodologies with Root Mean Squared Errors around 2% on average for 1000 duty cycles compared to between 2.64 to 7.27% for other state-of-the-art algorithms. We also show that the proposed methodology adapts to various cell chemistries and constructive configurations, and validate its applicability to a real-world scenario with experimental data from commercial LIBs.

1. Introduction

Since their commercialization in the early 1990s, Lithium-ion batteries (LIBs) have been widely used in key commercial and industrial applications, ranging from portable electronic and transportation to storage systems [1]. Unfortunately, the performance of LIBs declines with operation because of parasitic reactions taking place at the positive and negative electrodes (PE and NE respectively) as well as in the electrolyte [2,3]. In addition, specific side reactions such as lithium plating may create safety hazards [4,5]. Both performance decline and safety issues present a major concern for deployed LIB systems, particularly where long-lasting reliable applications are critical. To assess LIB performance and to overall ensure safety and reliability, the determination of the state of health (SOH) and/or state of charge (SOC) is required [6], and numerous methodologies have been proposed in the literature [7–9]. These methodologies can be based on testing (both invasive and non-invasive), physics-based models, data-driven approaches, and hybrid methods [7,10]. Each method provides a set of key advantages, drawbacks, and range of applicability [11]. Model-based techniques tend to be more accurate, although they require extensive prior knowledge and often invasive tests while only non-invasive techniques must be considered for application-oriented approaches. For this reason, data-driven methods have become popular in recent years, as they can model degradation features based solely on past records from which underlying causalities and correlations can be modeled [12]. Specifically, new methodologies based upon AI for the SOH [13,14] and SOC [15] have emerged thanks to the latest improvements in processor capabilities [16], communications [17,18], novel devices [19] and Artificial Intelligence (AI) [20,21]. It is expected that AI and Machine Learning (ML) approaches to compute SOH will have a profound influence on shaping the future LIB systems diagnosis and prognosis [22]. However, these methodologies are still in their early days [23–25] and critical issues remain to be addressed.

AI and Deep Learning (DL) have been exponentially applied to fields such as health [26], biology [27] or art [28]. Expansion of AI tools to such a wide range of fields has been possible because the problems to be solved can be highly abstracted from the field's domain. In battery research, however, this is not as easy as most problematics are technical and require an extensive knowledge of chemistry and physics [29].

Another barrier to the application of DL algorithms is the nature of the data. DL algorithms are typically oriented to work with 3 major categories: images, text and time series. For batteries, current, voltage and temperature records are usually obtained through measurements

* Corresponding author.
E-mail address: costanahuel@uniovi.es (N. Costa).

https://doi.org/10.1016/j.est.2022.105558
Received 24 May 2022; Received in revised form 16 August 2022; Accepted 24 August 2022
Available online 15 September 2022

over charge/discharge cycles or a mix of cycling time and calendar aging time. Accordingly, most Deep Learning-battery related papers take the available variables and apply time series-oriented neural networks, typically, Recurrent Neural Networks (RNNs), in order to predict capacity loss [30–36]. Unfortunately, this approach often does not allow satisfactory prognosis because of the possible nonlinearity of the capacity loss [37]. A SOH tracking method is only useful if it can predict or accommodate batteries with nonlinear degradations. This could be done by investigating variations of capacity vs. voltage curves or their derivatives (electrochemical voltage spectroscopies, EVS). EVS were proven extremely successful for prognosis of nonlinear degradations with the tracking of degradation modes [38,39] but, unfortunately, they do not use time series and thus do not fit into any of the 3 categories mentioned above. EVS are typically requiring constant current cycle to be applied properly. For most applications, this is done during a reference performance test which could be considered independent of the rest of the aging experiment. This makes EVS data similar to images because they provide an independent representation of the variations of capacity vs. voltage. Therefore, analyzing this type of data as images would allow the use of Convolutional Neural Networks (CNNs), which are powerful models that have been applied in many fields with remarkable results since they are able to automatically find distinctive patterns within images without the need for expert knowledge.

In addition to the growing sophistication of the needed algorithms, the amount of data needed for training and validation is also critical as battery data generation is challenging and time-consuming [40]. The reality is that existing datasets, while providing invaluable information, are scarce and only provide data for a few cells under limited testing conditions [40]. This is a major barrier to the application of DL algorithms, where large amounts of data are required for the training process. Furthermore, models trained on these datasets can lead to a false sense of confidence in their performance, as the capacity loss decays linearly in most cases and tests are usually carried on a low variety of duty cycles which are quite often disconnected from real applications (e.g., constant current cycling). Real data will be much more sporadic and sub and supra-linear degradation will be common. Moreover, since cells are different among datasets, the data cannot be compounded and knowledge from one dataset cannot be transferred to another [41].

Recent initiatives like battery archive [42] or battery data genome [29] should make data more available in the near future. In addition, the apparition of synthetic cycles [29,43–45] in the public domain could alleviate the shortage of data, and in particular the lack of variety in the duty cycles, as they can deliver data under an infinity of different degradation scenarios. A dataset consisting of millions of voltage vs. capacity curves with a complete spectrum of degradation for three major battery chemistries: $LiFePO_4$, Nickel Aluminum Cobalt Oxide, and Nickel Manganese Cobalt Oxide 811 was recently released [44] and will be used in this work. An important difference with respect to previous datasets is that this synthetic data not only provides information about capacity loss but also about degradation modes. This enables diagnosability [29] and opens the gate for informed prognosability [10].

Herein, we propose solutions to improve the application of DL algorithms to battery data. To this end, we sought a new representation of battery degradation data that would allow us to apply DL algorithms that have already been validated in other domains. Our representation consists of an image highlighting the differences between the EVS curves of a pristine and aged battery. Subsequently, we exploit the use of the HNEI's synthetic dataset [43] to train a Convolutional Neural Network (CNN) that predicts the battery health state based on its degradation mechanisms and not just capacity fade. This should enable the prediction of accelerated degradations. Finally, the adaptability of the method to deal with different cell configurations was validated with new synthetic data and subsequently on real cells.

2. Degradation mechanisms and degradation modes

Degradation in LIBs is the result of a complex interplay between physical and chemical mechanisms within the cell, that leads to capacity and power fade. Degradation is path-dependent and different usages (e.g., temperatures, load currents, duty cycles, depth of discharges, cut-off voltages, etc.) might inhibit or exacerbate specific degradation mechanisms [46,47]. Degradation mechanisms include solid electrolyte growth and decomposition, binder decomposition, graphite exfoliation, or grain isolation to name just a few [2,3,48]. Regardless of their origins and nature, the degradation mechanisms can only have a limited number of impacts on the electrochemical response [6,49]. These wide-ranging degradation mechanisms can be clustered into degradation modes, which are the loss of lithium inventory (LLI), the loss of active material (LAM) on the negative and positive electrodes (NE and PE respectively) and kinetic alterations.

Although degradation modes have been extensively reported in the literature [2,3,48], including experimental proofs [49], the underlying outcomes from the degradation modes on full cell effect are not always straightforward. For instance, LLI is generally the main source of degradation, is caused by parasitic reactions that consume lithium, is nearly always responsible for the entirety of capacity fade [49,50] and it can be modeled in half-cell configuration as NE "slippage" [51,52]. In contrast, LAM needs to be decomposed at the electrode or blend component level and is caused by changes in the availability of active mass for (de)intercalation. LAMs can be modeled as an individual "shrinkage" of the affected electrode or electrode components [50]. LAMs usually do not lead to a straight capacity loss in graphite-based batteries, hence that they may be referred to as "silent" or "hidden" modes. That is because LIBs yield an excess of relative capacity for each electrode outside the voltage window of the full cell. For the PE, that excess is the result of the NE lost during the SEI formation (i.e., the slippage) and of LLI. For the NE, that excess is there by design to protect against plating and it is also increased by LLI. Hence, most LAMs initially do not produce direct capacity loss, even if cell degradation is occurring. If LAMs eventually start to play a role in capacity loss, a second stage of accelerated aging arises [37]. The tracking and extrapolation of degradation modes were proven successful to forecast knees in the capacity loss [37].

Currently, several non-invasive testing methodologies to characterize battery degradation are available, including direct capacity testing characterization [53,54], high precision Coulomb counting [55,56], electrochemical impedance spectroscopy [57,58] and pulse power tests [59,60], or EVS [38,39]. In particular, the incremental capacity (IC) technique has been proven extremely successful [38,39] for quantifying degradation modes. EVS detects gradual changes in cell behavior with great sensitivity by studying the evolution of minute changes of the voltage response with cycling.

The relation between battery degradation and changes in the voltage response can be explained by changes in the electrode matching, i.e., how the PE and NE relate to each other and modeled using a mechanistic model. These models can be used to establish degradation mapping [61,62] that allows to select Features of Interest (FOIs) [61,63,64] which correspond to section of the signature especially sensitive to a specific degradation mode. Typical diagnosis methods must track FOIs and deconvolute their variations in detail to enable quantification of the degradation modes.

In most studies, this manual FOI tracking requires both an exhaustive analysis and expert knowledge. Data-driven methods could alleviate this issue and allow faster diagnosis by identifying patterns associated with degradation. However, data-driven methods are not always easy to implement and must be carefully designed to ensure the results have a physical meaning. For this reason, both expert knowledge and data-driven knowledge must evolve hand in hand. The first example of FOI analysis of large synthetic dataset was presented in [61]. Looking at data-driven methods, in [65] the dataset from [43] was used

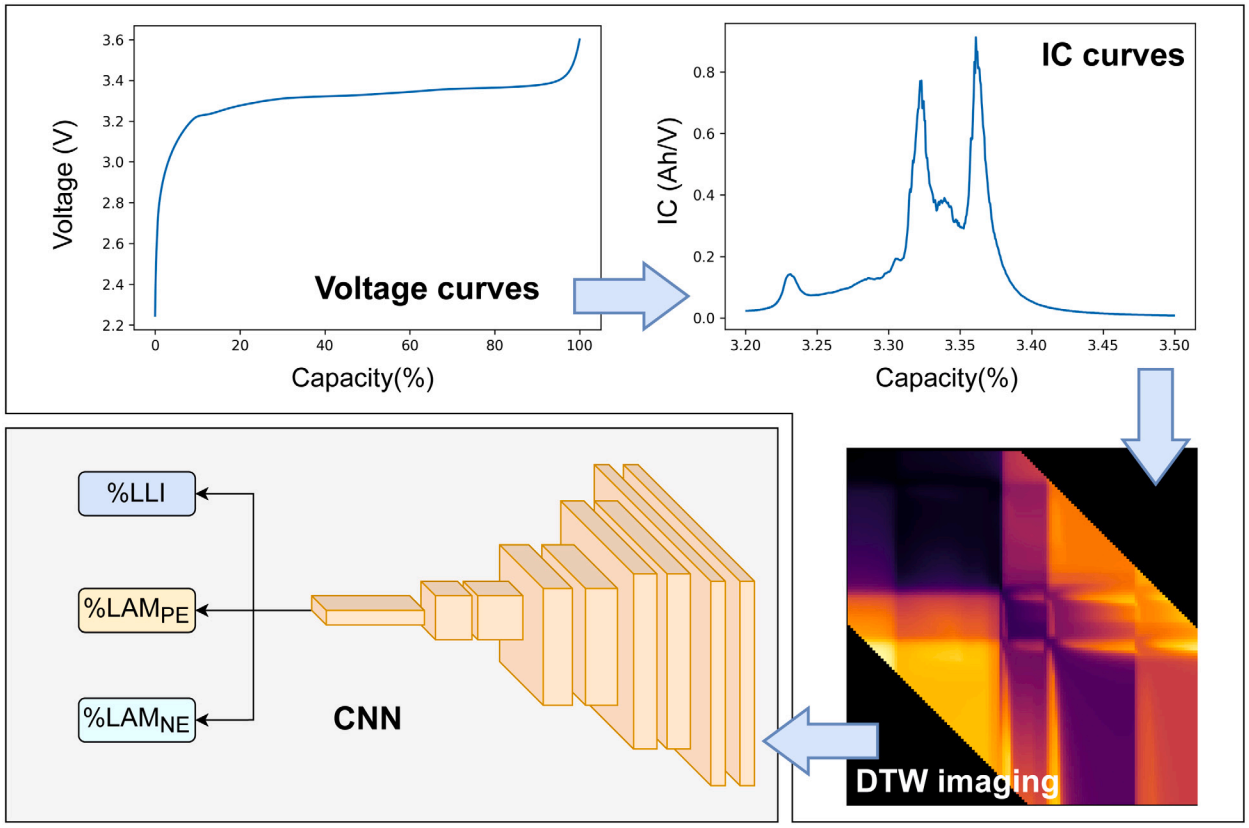

Fig. 1. Pipeline of the proposed solution. In the preprocessing step the IC curves are fed to the proposed algorithm to compute their representation as an image. Subsequently, the processed IC images are treated by a CNN that numerically quantifies the percentage of each degradation mode.

to train well-known Machine Learning methods such as Decision Trees and Random Forest regressors. In [45] the authors proposed a neural network composed of 1D convolutions for automatic classification and quantification of battery-aging modes. [66] proposed a method based on a simple multilayer feed-forward network for electrode-level Li-ion battery degradation diagnostics using EVS. The main limitation in these works is that the knowledge generated by the models cannot be extrapolated to new cell configurations. The method we propose aims to fill these gaps by transforming the voltage changes into images that reflect the degradation regardless of the cell configuration. This will create patterns that can be analyzed by traditional CNNs.

3. Deep learning approach

This section describes the proposed framework for material-based diagnosis in intercalation batteries (Li-ion and Na-ion). The process is summarized in Fig. 1 and consists of two separate steps. First, a pre-processing step, where charge data from the HNEI diagnosis dataset [43] is selected, converted to IC curves, and transformed into images. Second, a treatment step where the resulting images are used as inputs for a CNN trained to numerically identify and quantify the degradation modes.

3.1. Battery data to images — dynamic time warping

As stated in the introduction, one of the main difficulties towards AI to battery research is the type of data. Herein, this is circumvented by representing cell information as images. This opens up new opportunities for a consistent application of Deep Learning algorithms such as CNNs.

Dynamic Time Warping (DTW) [67] is an algorithm used to measure the similarity between two sequences. First, the Euclidean distance between each pair of points between the two sequences is calculated in a matrix. Among these distances different warping paths can be found, that is, possible deformations that a sequence should follow in order to be as similar as possible to the other. The method quantifies the similarity between the sequences by finding the best warping path, which corresponds to the one with the smallest accumulated distance. Fig. 2a presents the example of the application of DTW to two sine waves, referred to as Sin #1, located in the left part of the grid and Sin #2, located in the upper part of the grid, which shows a small deformation in the second period. The best path found in the matrix is marked in blue and indicates that for the Sin #2 to be the same as Sin #1, the deformation to follow is to slightly raise the values between 15 and 20. The similarity between the two sequences can be quantified with the resulting distance, i.e., the accumulated Euclidean distances of the path, which is 0.1946. At the lower left and upper right corners, the values are marked as inf (infinite) because there are no deformation paths that extend that far, so they are not calculated in order to reduce computation time. The method developed originally for speech recognition, and it is widely used for classification and clustering tasks [68–72].

DTW was already applied to the estimation of Li-ion battery capacity [73–75] as well as for augmenting the data obtained from different operating conditions [76]. However, these works make use of the similarities found in the best warping paths, rather than the full matrix representation. In this work, we propose for the first time to use the full matrix, represented as a set of pixels (see Fig. 2b) and thus as an image. Instead of sine functions, IC curves will be used as sequences, one pristine and one aged. IC curves were chosen over straight voltage vs. capacity curves because the derivation enhances small voltage variations and as a result will provide images with more details. An image can be generated for each sample in the dataset and each image will thus represent the similarity between the corresponding IC curve

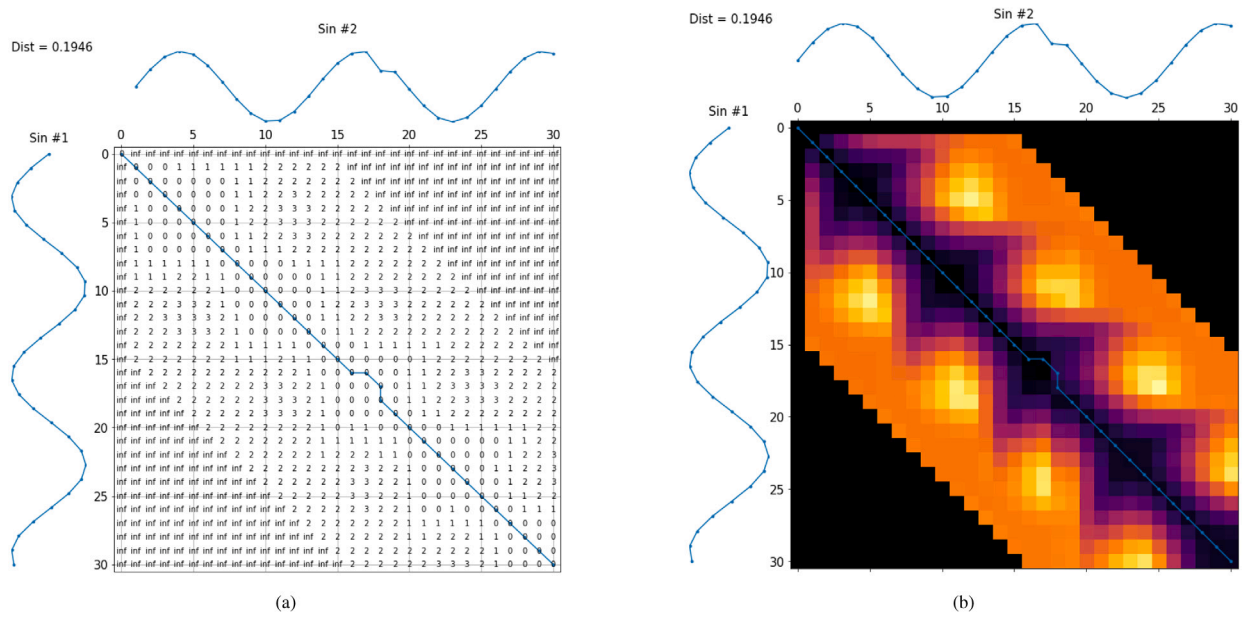

Fig. 2. Euclidean distance between each pair of points of the two sequences displayed on a grid (a). Every warping path represented as a set of pixels (b), note that the resolution depends directly on the length of the sequences, so the resulting image has the same resolution as the length of the sequences in (a), i.e., 30x30. In both images the optimal warping path is marked in blue. (For interpretation of the references to color in this figure legend, the reader is referred to the web version of this article.)

and the pristine one. Since each degradation path leads to a unique voltage response, it will also result in a unique image. As an example, Fig. 3 depicts the IC curves corresponding to 20% of each of the three degradation modes considered in the dataset: LLI, LAM_{PE} and LAM_{NE} (dashed lines) with the reference IC curve (solid lines) and their resulting images, labeled with the final DTW distance. This is to showcase that, just as the IC curves after different degradation are unique, the images are too. Straight IC curve plots cannot be used directly because they do not contain enough pixels with information. In our images, changes are reflected in shape, symmetry and colors. Note in the first degradation, LLI (Fig. 3a), the main peak located at 3.37 V is lost while in LAM_{PE} the peak that disappears is the minor one, located at 3.23 V. The images associated with these degradations also change, specifically in the intensity of the purple color, as well as in the symmetry, which is mainly lost in the first image, and consequently, the distance is greater, 0.77 vs. 0.31. In the LAM_{NE} degradation, the appearance of the peak at 3.45 V represents a sign of lithium plating in LFP cells [4]; On our image, this translates to the appearance of a lighter color band that coincides exactly with the position of the peak. The changes in this degradation are much more significant, and accordingly, the final calculated distance is greater: 1.53. In the end, just as with studying FOI variations, the degradation modes are decipherable from these unique images and so image processing algorithms such as CNNs can be undertaken.

A key property of these images is that they preserve the representation of the degradation modes regardless of the cell configuration. While the images were gathered from a dataset composed of synthetic curves, the differences between the pristine and aged IC curves should be similar for cells with slightly different cell configurations. In the mechanistic approach, a cell is defined by its active materials and two additional parameters, the loading ratio (LR), which corresponds to the electrode capacity ratio and the offset (OFS), which corresponds to their slippage compared to one another. Based on cell-to-cell variations studies [77], variations of LR by +/-0.2 and ΔOFS by +/- 2% were estimated possible within a batch. As an example, images associated with different cell configurations for the same degradation (20% of LLI) are presented in Fig. 4, with varied parameters to simulate cells from the same batch with slightly different properties (+/-0.01 for LR, +/-1% for OFS). Visually, the three images are almost identical and this is confirmed by the final DTW distance that were 0.65, 0.66, 0.62, respectively to be compared to the 0.77, 0.31, 1.53 for LLI, LAM_{PE} and LAM_{NE} degradations on Fig. 3. This is a key factor when applying the procedure to batteries with different operating modes or cell configurations, especially since batteries from the same batch have some cell-to-cell variations and batteries from different manufacturer might not use the same materials, additives or loading. This differentiates our method from other models trained on synthetic data that might not be applicable to real data.

It is noteworthy mentioning that the resolution of the data used in this work is of 1001 points over the voltage window. To reduce computation time calculating the images the resolution was downscaled to a point every 2.3 mV per IC curve using a 1-D monotonic cubic interpolation with the Scipy Pchip Interpolator [78]. This kept the main features of interest intact while limiting the file size. As a result, the generated images, Figs. 3 and 4 included, are of 128 by 128 pixels. The dtaidistance package [79] was used to compute the DTW matrix.

3.2. Model

With the new approach for the generation of high-quality training data established, attention can be set to the DL model. DL methods are sophisticated ML approaches that can handle high-dimensional data and are capable of automatically capturing underlying features to make accurate predictions. Convolutional Neural Networks (CNN) are a subset of DL models that are particularly well-suited for image recognition tasks and with multiple derived architectures such as AlexNet [80], U-NET [81] or the recent vision transformers [82].

CNNs consist of multiple layers of neurons. The structure of the proposed model is depicted in Fig. 5. The detailed description of each layer is as follows:

- Masking layer: this layer is used to mask data to be omitted by the next layer. In the DTW matrix, paths farther away from the diagonal lose importance (the inf values) and can be omitted.
- Convolutional layers (Conv1 to Conv4): these layers are composed each of a conv2D layer (light orange) and a Max-Pooling

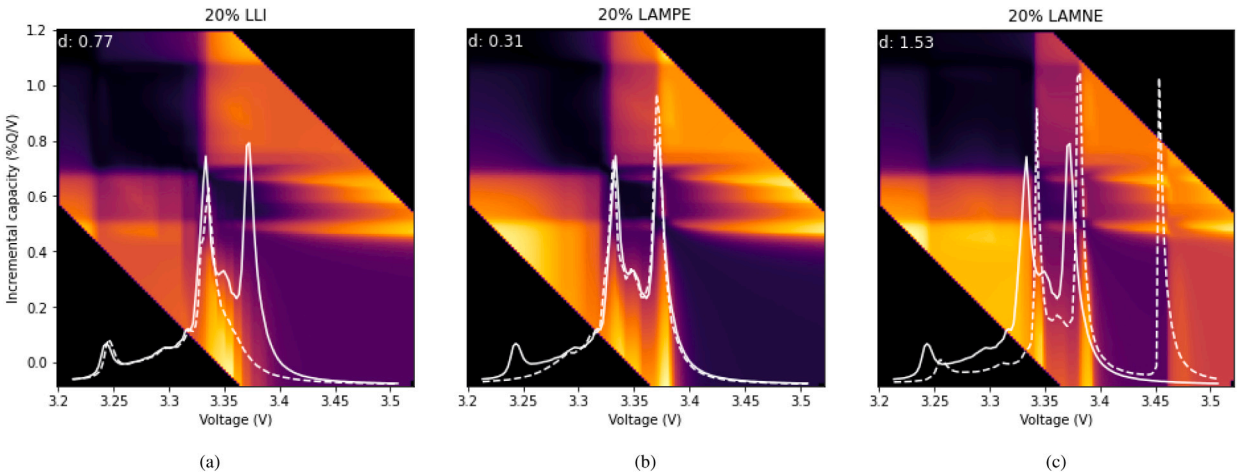

Fig. 3. IC signatures from the initial state (solid line) for each degradation in the dataset: LLI (a), LAMPE (b) and LLI(c) at 20% degradation (dashed line) together with the associated DTW image. (For interpretation of the references to color in this figure legend, the reader is referred to the web version of this article.)

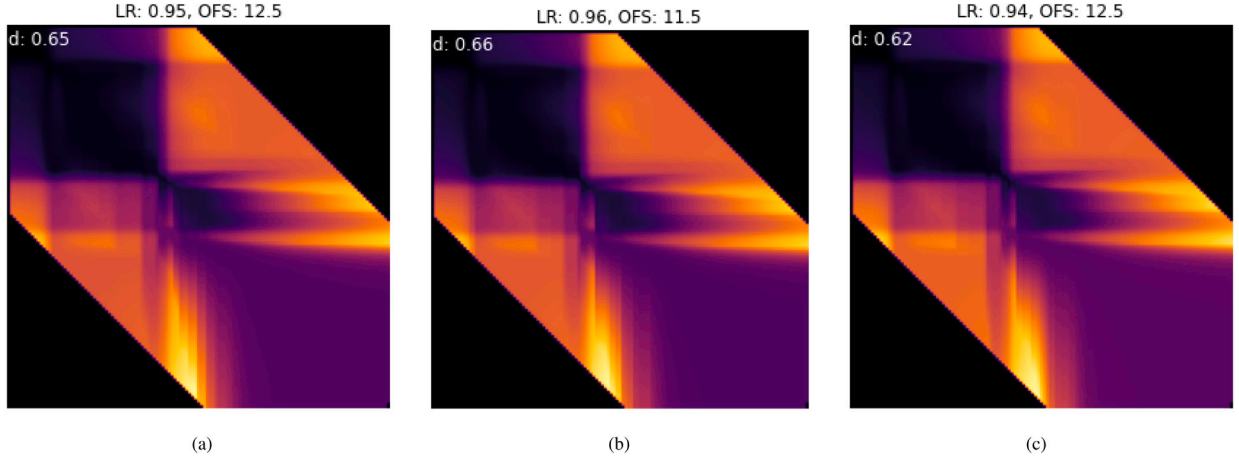

Fig. 4. DTW images for 20% LLI degradation for three different cell configurations.

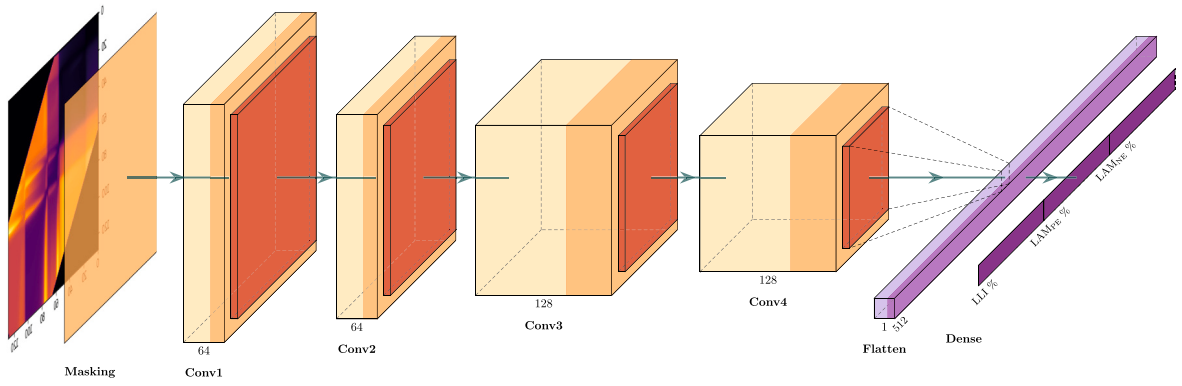

Fig. 5. Model architecture. Conv1 to Conv4 represent the convolution layers followed by the max pooling layers. The features extracted are condensed in a flattened layer from which the 3 degradation modes are predicted. (For interpretation of the references to color in this figure legend, the reader is referred to the web version of this article.)

layer (dark orange). The conv2D layers consist of multiple filters, which are applied to the image to highlight certain features that make the image unique such as the direction of the lines or their shape. The resulting images are known as feature maps. 64 filters are applied in each of the first two layers to obtain the features maps that mainly characterize the image, while in the last two layers more filters are needed (128 each) to capture finer details like color intensity or brightness. The Max-Pooling layer reduces the spatial size of the feature maps and learns to ignore irrelevant and redundant information, that is why the dimension of the blocks is reduced in each layer.

- Flatten layer: after the convolution and max pooling flow, the shape of the matrices is flattened to a single vector containing all the information needed for predictions.

- Dense layer: this layer applies a sigmoid activation function to obtain a value between 0 and 1 representing the percentage prediction of each of the degradation modes.

The activation function used after every convolution is ReLU and also a dropout layer was included to randomly set input units to 0, which can generally help to prevent overfitting. Nevertheless, we found that including this layer led to a premature regularization and as a result to a sub-optimal model, therefore it was not used in the final model.

The WandB framework [83] was used to find the optimal configuration of filters and layers. In addition, to achieve the best possible performance of our model, callbacks to relegate the training stop condition to the validation error were used instead of the number of epochs.

In summary, each sample in the dataset consists of an image reflecting the differences between an aged IC curve and the pristine one. These images, along with the associated diagnosis, are fed to the model which learns the features that characterize each type of degradation and then compress all the knowledge in the last layer to predict the percentages of each degradation mode.

4. Experimental design

The training data used in this work is publicly available [44] and is composed of more than 700,000 unique voltage vs capacity C/25 charge curves each for LFP, NMC, and NCA. They were generated with different combinations of LLI, LAM_{PE} and LAM_{NE} at a resolution of at least 0.85% between 0 and 85%, encapsulating the full spectrum of degradation. The resulting capacity losses were capped to 85%.

The end of life (EoL) of a battery is usually driven by the application, however, usage after 40% capacity loss is rarely allowed. In practice, the benefit of diagnosing a battery lies in predicting its remaining useful life or, if it is partially deteriorated, knowing whether it can be put to a second use. Since our goal is to provide a methodology to detect subtle evidence to forecast durability, data above 40% capacity loss was not used for training.

The choice of the testing data was carefully made. To statistically validate the performance of a ML algorithm, it is common to divide the data into two independent parts: the first is used for training and the second for testing. A possible approach would be to consider one resolution for the training set and another for the test set to test the interpolation capability of the model. The main drawback of such a setting is that the test set is a sparser subset of the same initial data, therefore training is not as complete as it could have been and test sets are not independent. As a consequence, the model accuracy may be optimistic because samples in the test set are close to those in the training set, a well-known problem in ML called overfitting [84].

To avoid this problem and to differentiate whether the model has actually learned the degradations we elected to calculate new synthetic data sets for each of the chemistries with slightly different configurations than the cells in the training sets. This allows having completely independent training and validation sets to provide a benchmark for the fair and equal evaluation of different ML models. Details about the test sets, each consisting of 1000 duty cycles, can be seen in Table 1. Fig. 9(a) in Appendix A shows the capacity losses associated with the duty cycles calculated in [44]. As prognosis is the ultimate goal, we decided to select a 1000 subset of these duty cycles to provide a test set that can be used both for diagnosis (as is the case of this work) and for prognosis (for future works). Combinations of the [LLI, LAM_{PE}, LAM_{NE}] degradations were selected to generate the duty cycles for the new cell configurations to show a wide range of both sublinear and supralinear degradations. Emphasis is placed on the latter due to their interest in identifying knees in capacity loss, correlated with the so-called silent modes. Calculations are done for the following cycles: 10, 50, 100, 200, 400 and 1000 (Fig. 9(c)) with capacity losses up to 40% (Fig. 9(d)).

Table 1
Details about test sets. Three cells, labeled as C1, C2, C3, were generated using the 'alawa toolbox [50] for each chemistry. The values of LR (Loading Ratio) and OFS (offset) with which they were generated are included. Parameters used for the training data are also added to highlight the differences with respect to the test sets.

	Training data		C1		C2		C3	
	LR	OFS	LR	OFS	LR	OFS	LR	OFS
LFP	0.95	12.5	0.96	11.5	0.94	12.5	0.95	11.5
NCA	1.05	1.5	1.06	0.5	1.04	2.5	1.05	0.5
NMC	0.90	10	0.91	9	0.89	11	0.90	9

5. Results

The experimental validation of the proposed framework will be performed first on synthetic data, then on real data. In both cases, our framework will be compared to the state-of-the-art for degradation modes quantification. The metric chosen for evaluation, defined in Appendix B, is the Root Mean Squared Percentage Error (RMSPE).

5.1. Validation on synthetic cycles

In this section, the performance of our method was compared to state-of-the-art methods apple to apple using the same synthetic dataset with different cell configurations.

Results for degradation mode quantification for all methods are presented in Tables 2 and 3 for the LFP cells. Results for NCA and NMC are included in Appendix C.1. Among the tested methods were the works described at the end of Section 2 and the one described in this work, labeled in the tables as "RF" for the Random forest Regressor [65], "1DConv" for the 1D convolutional neural network [45], "FNN" for the Feed-forward neural network [66] and "DTW-CNN" for our Dynamic Time Warping-convolutional neural network approach. It should be noted that only our method uses DTW images while the other approaches use the IC curves directly. In addition, a CNN is also used in [45], but 1D convolutions are applied, which are not suitable for images. These methods did not provide any public code implementation, consequently, the steps described in their corresponding papers were followed to reproduce their models adapted to these test sets (see Appendix C.2 and https://github.com/NahuelCostaCortez/DTW-Li-ion-Diagnosis for details). Table 2 lists the diagnosis accuracy (by the means of RMSPE values) for the quantification of the three degradation modes at six different cycles (10, 50, 100, 200, 400 and 1000) for the three different LFP cell configurations (C1 to C3 in Table 1). The best predictions are highlighted in bold. Overall, the approach presented in this work clearly outperforms the others with an average error of 2.00% (see Table 3). Yet, there are certain cycles where other methods perform slightly better. This may be due to some bias during training that may lead to unbalanced predictions and, as a consequence, to reasonable performance in one degradation mode but not in the others. For instance, the predictions of "1DConv" for cycle 400 in C1. Numerically in LAM_{PE} it has a better result than our approach (3.38% vs 3.59%), however for LLI (1.68% vs 1.31%) and especially for LAM_{NE} (2.83% vs 1.93%) the performance is considerably worse. This is quickly identified in the standard deviation, where our model with a value of 1.96 shows a lower dispersion compared to the other models. Tables 4 and 6 in Appendix C.1 present the same analysis for the NCA and NMC cells, respectively. The results are similar with an average error of 2.03% (see Table 7) for NMC, compared to errors from 2.56 to 7.27% for the other methods. The approach seems to perform better for NCA cells with an average error of 1.11% (see Table 5), compared to errors from 1.31 to 7.01% for the other methods.

The main reason behind the consistent estimations in our approach is that the representation of degradations in the images is largely preserved between different cell configurations, something that is not the case in pure IC curve processing, where peaks, despite having similar

Table 2
RMSPE results for each degradation mode and cycle for the LFP test set.

		LLI						LAMPE						LAMNE					
	C1	1.89	1.93	2.00	1.82	1.67	3.91	2.53	2.90	3.09	3.28	3.58	11.11	2.30	2.32	2.32	2.10	2.15	6.31
FNN [66]	C2	2.06	2.16	2.23	1.81	1.55	3.67	3.30	2.94	2.94	2.73	3.46	11.32	3.41	3.29	3.28	2.77	2.35	6.19
	C3	1.45	1.93	1.88	1.68	1.73	4.02	2.27	3.14	3.40	3.52	3.78	11.31	3.04	3.06	2.98	2.64	2.44	6.37
	C1	6.32	5.69	4.94	3.62	3.23	9.21	5.89	5.13	4.26	3.15	5.16	9.13	7.00	6.06	5.02	3.82	6.24	11.83
RF [65]	C2	6.32	5.69	4.94	3.64	3.14	9.22	5.89	5.13	4.26	3.17	4.97	9.79	7.00	6.06	5.02	3.82	6.38	11.55
	C3	6.32	5.69	4.94	3.62	3.20	9.13	5.89	5.13	4.26	3.15	5.07	9.37	7.00	6.06	5.02	3.82	6.18	11.66
	C1	1.18	0.95	0.73	**1.06**	1.68	3.21	1.90	1.23	**1.80**	2.80	**3.38**	10.73	1.18	1.33	**1.27**	**1.71**	2.83	6.60
1DConv [45]	C2	0.63	**0.59**	**0.86**	**1.11**	1.62	3.15	**0.41**	**1.28**	2.76	2.62	**3.50**	10.85	2.05	1.83	2.03	2.36	2.86	6.58
	C3	1.95	0.89	0.60	0.96	1.75	3.35	**2.08**	**1.15**	**2.01**	2.95	**3.44**	10.86	2.86	1.97	1.59	2.07	2.93	6.61
	C1	**0.14**	**0.53**	**0.72**	1.16	**1.31**	**2.47**	**0.96**	**0.98**	1.82	**2.67**	3.59	**8.64**	**0.17**	**0.70**	1.40	1.98	**1.93**	**3.86**
DTW-CNN	C2	**0.44**	0.84	0.91	1.18	**1.32**	**2.15**	0.78	2.06	**2.76**	**3.22**	3.92	**8.89**	**0.21**	**0.57**	**0.80**	**1.11**	**1.41**	**4.01**
	C3	**0.80**	**0.56**	**0.56**	**0.95**	**1.12**	**2.58**	2.30	1.32	2.03	**2.72**	3.67	**8.63**	**0.59**	**0.55**	**1.00**	**1.43**	**1.64**	**3.94**
		10	50	100	200	400	1000	10	50	100	200	400	1000	10	50	100	200	400	1000

Table 3
RMSPE results summary for the LFP test set calculated as the average and the standard deviation of predictions in all cycles for all cells.

	FNN	RF	1DConv	DTW-CNN
Mean ± std	3.32 ± 2.21	5.87 ± 2.23	2.64 ± 2.42	**2.00 ± 1.96**

morphologies, suffer from shifts that can cause models to misleading predictions.

The method performs remarkably well and surpassed the tested state-of-the-art approaches; however, it still has room for improvement. For instance, note the large errors in later cycles (400 and 1000), which correspond to degradations around 40% of capacity loss. Although these errors are still much lower than in the other methods the estimations for these cycles could be further improved. Some other comparative tests could also be added to the discussion; however, the main objective of this work was to enable the use of images to exploit the potential of CNNs. We have developed and used one of the many architectures that can be found in the literature, but predictions could be improved by other newer and more robust models. Furthermore, the key factor, and in fact, one of the essential features of Deep Learning, is precisely reusability. The knowledge of large models trained on a specific task can be transferred to a new, similarly related task. This is known as Transfer Learning [85] and is especially useful when little data is available, instead of training a model from scratch it can leverage the knowledge generated by a pre-trained model for fine-tuning on the available data. This technique is mainly focused on images, therefore the preprocessing we propose, besides providing an adaptive method, also allows the application of this technique: we have pre-trained a large model on the training set (DTW-CNN), so its knowledge can be now used by other models on the test sets or on new data. This path, as well as other complementary ones such as the explainability of the models or the choice of the CNN architecture, will be explored in future work.

Finally, to demonstrate the performance of the model in a more realistic application context, we provide a demo in https://huggingface.co/spaces/NahuelCosta/DTW-CNN. The cycles associated with the three LFP test cells can be selected to display their IC curves, the corresponding DTW image and the final diagnosis given as the percentage of each predicted degradation mode.

5.2. Validation on real battery data

As demonstrated above, one of the strengths of the model is its applicability to cells with configurations other than those seen during training. This also includes real cells so in this section our model was tested on cycling data from two commercial high-power graphite//LFP cells manufactured by A123 Systems (ANR26650M1, 2.3 Ah) that have been previously studied. The cells will be referred as CReal#1

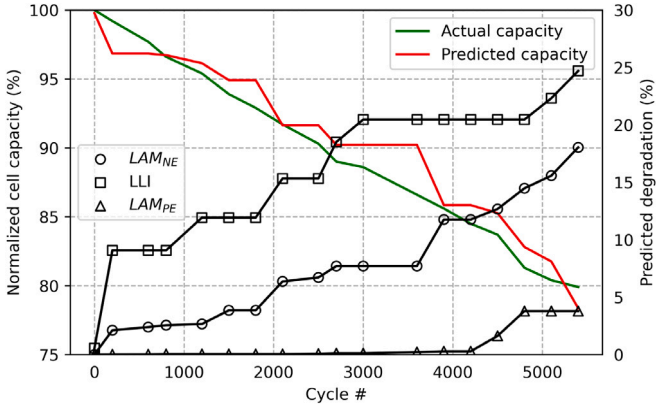

Fig. 6. Model predictions for Cell#1 for every available cycle.

and CReal#2 for simplicity; CReal#1 was tested under multistage fast charging [86] while CReal#2 was tested under dynamic stress test (DST) driving schedule [38]. In these studies, the degradation modes were quantified using the 'alawa toolbox [50]. It should be noted that the toolbox uses the same mechanistic model than the one that generated the training data used in this study. Therefore, in the end, the predictions of our model are an automatic way of making the same diagnosis without relying on prior knowledge in the field.

CReal#1 was cycled to simulate fast charge and discharge conditions. Every 300 cycles, a reference performance test (RPT) was done to determine the state of health (SOH) of each cell. Fig. 6 shows the model predictions for each of the voltage curves of the available cycles. The diagnosis established by our model in terms of degradation mode quantification and capacity loss estimation matched the experimental observations. The capacity estimation adjusted remarkably well to the evolution along the cycles and for the degradation modes, despite some fluctuations, they tended to follow a linear degradation with LAM_{NE} and LLI being the main actors, while the effect of LAM_{PE} is almost negligible. These predictions meet the results reported in [86], where the degradation was concluded to be caused by a linear loss of LLI of 0,0032% per cycle followed by a linear loss of LAM_{NE} of 0,0022%.

CReal#2 was cycled differently to study the impact of fast charge with an EV type discharge rather than constant current. The degradation path was quite different than of CReal#1 and significant Li plating occurred. Plating is considered one of the most detrimental phenomena in lithium-ion batteries, as it increases cell degradation and might lead to safety issues. RPTs were again performed every 300 full DST cycles. Model predictions are presented in Fig. 7 together with the diagnosis reported in [38]. Despite the few cycles available, the capacity estimation is quite correct. Looking at the degradation modes, their evolution is more complex than of CReal#1. LAM_{NE} is calculated

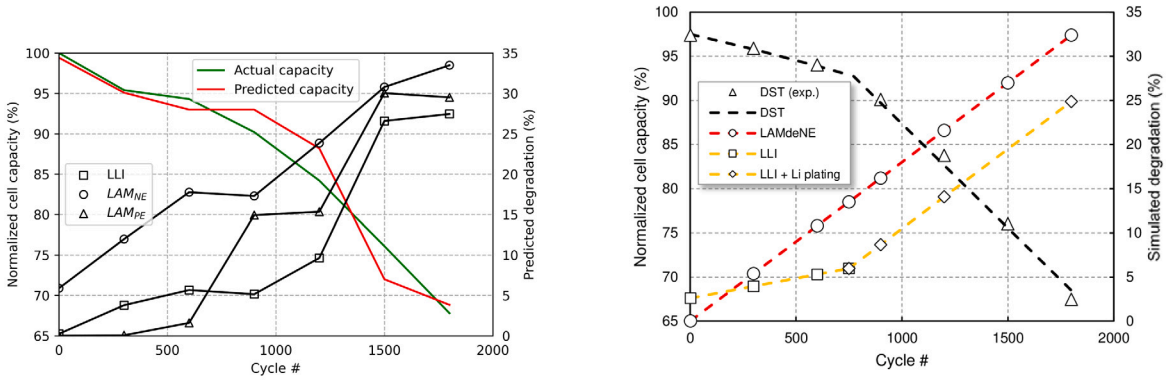

Fig. 7. Model predictions for Cell#2 for every available cycle (a). Diagnosis estimated in [38] (b).

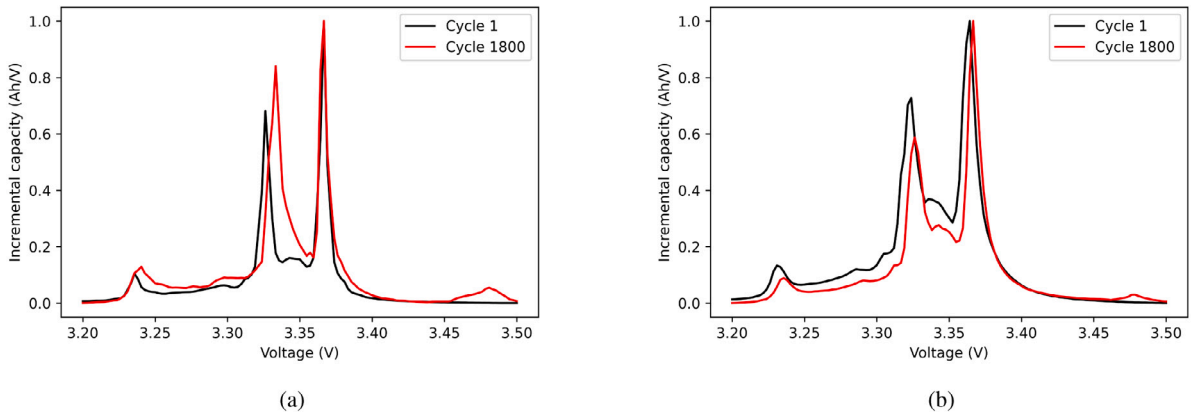

Fig. 8. IC curves for cycles 1 and 1800 in the real cell (a) and in the synthetic cell generated for the predicted degradation percentages (b).

Table 4
RMSPE results for each degradation mode and cycle for the NCA test set.

		LLI						LAMPE						LAMNE					
	C1	**0.13**	0.69	1.05	1.17	0.89	**1.19**	1.27	1.66	1.55	1.67	1.78	**1.41**	**0.21**	1.10	2.01	2.37	**1.82**	**2.48**
FNN [66]	C2	**0.11**	**0.51**	**0.67**	0.81	0.82	1.30	0.52	0.64	0.76	0.87	0.84	1.09	0.19	1.21	2.18	2.96	2.56	2.87
	C3	0.16	0.62	0.90	1.04	0.77	**1.19**	1.98	1.51	1.36	1.45	1.52	1.19	**0.19**	1.20	2.28	3.07	2.47	**2.72**
	C1	5.58	8.58	8.04	8.65	8.90	9.35	5.08	7.77	7.10	7.15	6.55	11.58	5.64	5.82	4.82	4.63	7.16	13.34
RF [65]	C2	4.58	4.41	5.67	6.81	7.87	9.23	4.16	3.93	4.95	5.61	6.41	11.68	5.40	4.56	4.07	3.8	7.35	13.75
	C3	5.43	7.53	6.97	8.05	8.71	9.29	4.95	6.76	6.13	6.60	6.73	11.58	5.60	5.42	4.50	4.12	6.82	13.48
	C1	0.32	**0.33**	**0.56**	**0.77**	**0.80**	1.5	2.31	2.07	2.05	2.01	1.90	1.43	0.37	**0.74**	**1.36**	1.99	1.95	3.06
1DConv [45]	C2	0.33	0.42	0.44	**0.53**	**0.69**	**1.10**	0.94	0.79	0.83	0.82	**0.79**	**0.87**	**0.22**	1.09	1.69	2.56	2.77	3.44
	C3	0.34	**0.36**	**0.47**	**0.68**	**0.71**	1.36	2.08	1.74	1.72	1.67	1.57	**1.18**	0.20	1.01	1.75	2.69	2.68	3.37
	C1	0.35	0.34	0.56	0.99	1.43	2.36	**0.47**	**0.64**	**0.67**	**0.96**	**1.41**	2.06	1.79	1.50	1.40	**1.41**	1.52	2.57
DTW-CNN	C2	0.69	0.93	1.03	1.24	1.80	1.93	**0.21**	**0.43**	**0.63**	**0.73**	0.94	1.43	0.27	**0.69**	**0.78**	**1.06**	**1.37**	**2.68**
	C3	**0.12**	0.44	0.72	0.97	1.28	2.05	**0.60**	**0.40**	**0.65**	**1.03**	**1.40**	2.00	0.40	**0.59**	**0.69**	**1.00**	**1.39**	3.16
		10	50	100	200	400	1000	10	50	100	200	400	1000	10	50	100	200	400	1000

as linear with a higher slope than of CReal#1. LLI started linear and then accelerated after 700 cycles. LAM_{PE} evolution fluctuates a lot but seems rather linear with a much higher slope than of CReal#1. The overall evolution of the degradation modes matched quite well the analysis performed in [38] where the high pace of LAM_{NE} induced some Li plating of which most passivated in LLI. The main difference is the LAM_{PE} estimation. LAM_{PE} is extremely difficult to quantify for LFP type cells as was considered in [38] as it was inducing neither capacity loss nor was at the origin of the knee.

In contrast, our model took every possible degradation into account during training and predicted some LAM_{PE}. The true extend of it could not be verified on the electrochemical data as no post-mortem study was carried on the aged cell. Fig. 8 shows the IC curves for cycles 1 and 1800 in the real cell and in the synthetic cell generated for the predicted degradation percentages. It is expected that the curves will not be exactly the same due to the differences between the simulation and the real data, the interest lies in the peak appearing at around 3.47 V, which is known to imply some reversible plating in the cell.

Table 5
RMSPE results summary for the NCA test set calculated as the average and the standard deviation of predictions in all cycles for all cells.

	FNN	RF	1DCov	DTW-CNN
Mean ± std	1.31 ± 0.77	7.01 ± 2.51	1.32 ± 0.86	**1.11 ± 0.67**

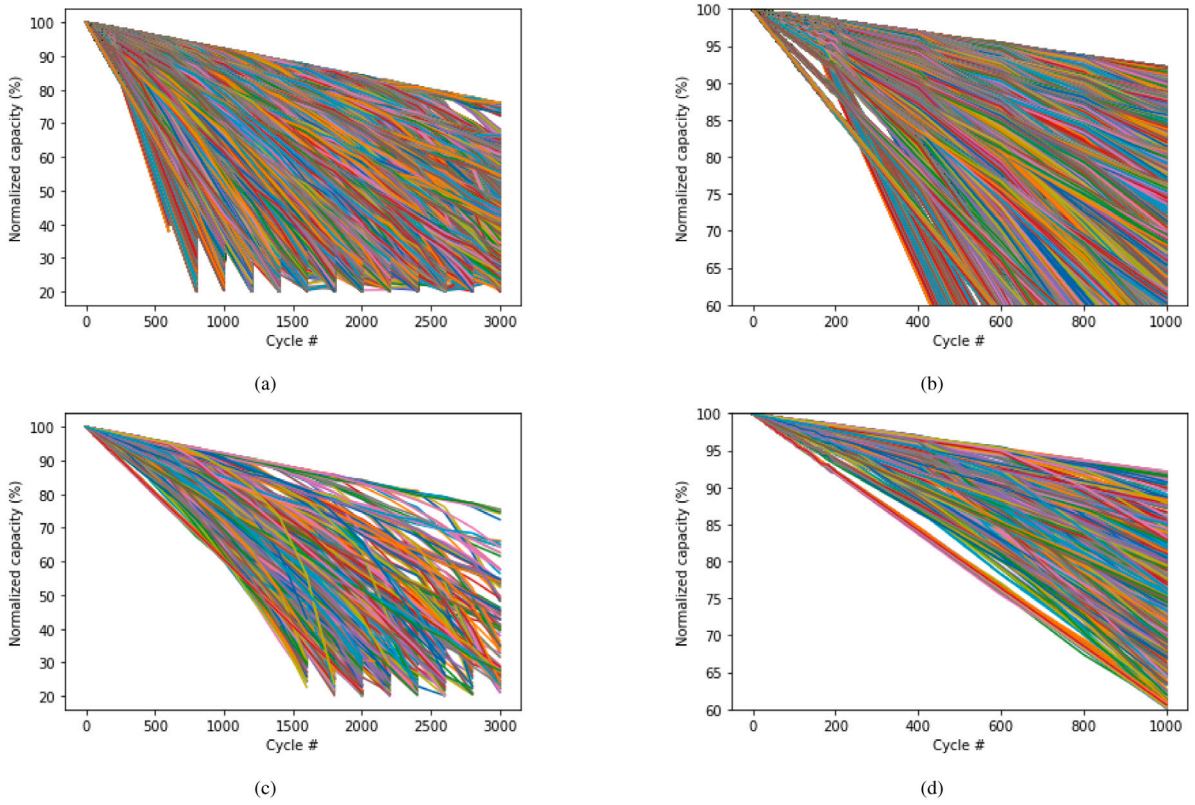

Fig. 9. Evolution of capacity loss over the 127662 duty cycles presented in [44] for the LFP cell (a). Same plot as in (a) for the first 1000 cycles and at 60% of capacity (b). Evolution of capacity loss over the 1000 duty cycles selected for test (c). Same plot as in (c) for the first 1000 cycles and at 60% of capacity (d).

Table 6
RMSPE results for each degradation mode and cycle for the NMC test set.

		LLI						LAMPE						LAMNE					
	C1	**0.39**	0.48	0.84	1.18	**2.00**	**2.12**	3.02	3.57	3.54	3.28	2.98	**3.08**	**0.26**	1.16	2.27	**3.68**	**4.91**	**7.18**
FNN [66]	C2	2.71	2.60	2.48	2.25	**1.91**	**2.34**	1.29	1.24	1.51	1.30	1.21	2.41	5.43	5.30	5.12	4.77	5.07	8.23
	C3	**0.29**	**0.30**	0.60	0.93	1.91	**1.99**	2.69	2.90	3.09	2.95	2.69	**2.97**	**0.17**	1.11	2.20	3.43	4.51	**6.76**
	C1	8.30	7.52	6.57	4.83	3.79	11.41	6.91	6.16	5.29	3.96	5.96	9.42	9.25	8.37	7.35	5.72	5.62	14.37
RF [65]	C2	8.30	7.52	6.57	4.83	3.49	11.68	6.91	6.16	5.29	3.96	5.36	8.96	9.25	8.37	7.35	5.72	5.63	15.26
	C3	8.30	7.52	6.57	4.83	3.73	11.41	6.91	6.16	5.29	3.96	6.11	9.54	9.25	8.37	7.35	5.72	5.67	14.25
	C1	0.47	**0.40**	**0.52**	0.73	1.23	2.68	4.01	4.02	3.95	3.83	3.91	3.60	0.29	1.18	2.11	3.02	3.75	7.82
1DConv [45]	C2	1.96	2.00	1.94	**1.72**	1.59	2.47	0.57	0.38	**0.41**	0.48	**1.14**	**1.80**	4.54	4.35	4.33	4.39	4.84	7.91
	C3	0.47	0.35	**0.54**	0.70	1.27	2.76	**3.90**	3.74	3.61	3.55	3.54	3.34	0.19	1.03	1.80	2.43	**3.17**	7.36
	C1	0.65	0.67	0.72	**0.64**	**0.96**	4.32	1.70	**1.92**	**1.99**	**1.92**	**2.29**	**3.91**	0.44	**0.48**	**1.06**	**2.18**	**3.55**	**7.58**
DTW-CNN	C2	**1.00**	**1.00**	**0.82**	**0.74**	**1.23**	3.00	**0.80**	**0.59**	0.52	**0.86**	2.36	**4.54**	**2.19**	**1.94**	**1.71**	**1.91**	**2.91**	**7.48**
	C3	0.76	0.90	0.82	**0.64**	**1.17**	4.47	1.86	**2.03**	**2.00**	1.85	**2.05**	3.78	0.77	**0.79**	**0.93**	**1.82**	3.28	7.37
		10	50	100	200	400	1000	10	50	100	200	400	1000	10	50	100	200	400	1000

Table 7
RMSPE results summary for the NMC test set calculated as the average and the standard deviation of predictions in all cycles for all cells.

	FNN	RF	1DConv	DTW-CNN
Mean ± std	2.68 ± 1.81	7.27 ± 2.66	2.56 ± 1.90	**2.03 ± 1.72**

Hence, model predictions also suggest that the occurring degradation mechanism is irreversible lithium plating.

All things considered, it appears that the model adapted well to conditions different from those seen during training, with the predictions meeting to a large extent the previous diagnosis. Since different combinations of degradation modes can lead to the same capacity loss, which gives room to confusion in results interpretation, the model needs not only to estimate a concrete percentage of the degradation modes to offer a possible range of degradations with a certain degree of confidence. This only can enable prognosis [44], which will be the topic of future work.

6. Concluding remarks and future work

Data-driven methods are a promising avenue for lithium-ion battery diagnostics and prognostics. Thus, efforts to use AI for state estimation and lifetime prediction have emerged in recent years. However, the application of modern AI algorithms is still at an early stage. In this work, we proposed a novel method for battery degradation diagnosis, that represents battery data as images, with the aim of enabling the use of powerful AI models in this domain. Especially, the IC curves from HNEI's synthetic datasets were used to train a CNN that successfully predicts the main degradation mechanisms on several commercial cells of different chemistries and with different characteristics. The performance of the model was compared to other state-of-the-art methods, where the superiority of our approach was clearly demonstrated, with

Table 8
Configurations of the models used. In [66] and [45] "layers config" refers to the number of neurons per layer. Also, in [45], the authors built a 1D CNN to quantify LLI only while here we used the same model to predict the three degradation modes.

Method	Hyperparameters		
FNN [66]	*num_layers* 3	*layers* Fully Connected layers	*layers config* 64 × 32 × 3
RF [65]	*max_depth* 10	*random_state* 42	*n_estimators* 100
1DConv [45]	*num_layers* 5	*layers* 2 1D CNN layers and 3 Fully Connected layers	*layers config* 32 × 32 × 128 × 64 × 3

RMSPE errors around 2% in average for 1000 duty cycles compared to between 2.64 to 7.27% for the other tested methods. The successful performance of the model is largely due to its adaptive nature to different cell configurations. To validate this claim, the model was also tested on real cells, where the diagnosis corresponded to a large extent with previously existing studies on the subject. This opens up new opportunities for collaboration between AI and battery research.

In future works we aim to explore the use of Transfer Learning as well as the suitability of the approach for prognosis, evaluating the evolution of the peaks throughout the cycles, rather than independent cycle diagnosis. In addition, for this study the data used were only from charge cycles, however, considering discharge data is also of great interest for a more complete diagnosis. Lastly, our interests are aligned with the extension of the study of degradation modes, a key subject to contribute to the electrochemical understanding of cell deterioration.

CRediT authorship contribution statement

N. Costa: Conception and design of study, Analysis and/or interpretation of data, Writing – original draft, Writing – review & editing. **L. Sánchez:** Writing – original draft, Writing – review & editing. **D. Anseán:** Writing – original draft, Writing – review & editing. **M. Dubarry:** Conception and design of study, Acquisition of data, Writing – original draft, Writing – review & editing.

Declaration of competing interest

The authors declare that they have no known competing financial interests or personal relationships that could have appeared to influence the work reported in this paper.

Data availability

The data used in this study is available for download. LFP: http://dx.doi.org/10.17632/bs2j56pn7y.3 and http://dx.doi.org/10.17632/6s6ph9n8zg.3, NCA: http://dx.doi.org/10.17632/2h8cpszy26.1, NMC: http://dx.doi.org/10.17632/pb5xpv8z5r.1.

Acknowledgments

This work has been partially supported by the Ministry of Economy, Industry and Competitiveness ("Ministerio de Economía, Industria y Competitividad"), Spain from Spain/FEDER under grant PID2020-112726-RB-I00 and by Principado de Asturias, grant SV-PA-21-AYUD/2021/50994. M. D. is thankful to the Office of Naval Research, USA APRISES grants N00014-18-1-2127 and N00014-19-1-2159 for funding. All authors approved the version of the manuscript to be published.

Appendix A. Duty cycles selection

See Fig. 9.

Appendix B. Model evaluation

In regression problems, the Mean Absolute Error (MAE) and Root Mean Squared Error (RMSE) metrics, or their versions expressed as a percentage MAPE and RMSPE are commonly used. MAE measures the mean magnitude of errors in a set of model estimates while RMSE is the root of the averaged quadratic score. In RMSE the errors are squared before averaged, whereas in MAE all individual differences are equally weighted in the mean. This makes RMSE more sensitive to large errors. Consequently, RMSE is considered more effective for testing model performance, especially when large errors are undesirable. For simplicity in the interpretation of results, RMSE expressed as a percentage (RMSPE) is chosen:

$$RMSPE = \sqrt{\frac{1}{N}\sum_{i=1}^{N}\left(\frac{y_i - \hat{y}_i}{y_i}\right)^2} \times 100 \quad (1)$$

(number of samples; predicted value; real value)

However, using this metric requires dividing the prediction error by the actual value. In the dataset used in this problem, there are combinations where the actual value (the degradation mode) is simply 0, so the calculation would be invalid. Because of this, the denominator is replaced by the nominal capacity of the cell understood as the initial capacity expressed in percentage, i.e., 100%. Predicted values are already given in percentages (for the degradation modes) therefore the definitive metric used is:

$$RMSPE = \sqrt{\frac{1}{N}\sum_{i=1}^{N}\left(y_i - \hat{y}_i\right)^2} \quad (2)$$

(number of samples; predicted value; real value)

Appendix C. Supplementary tables

C.1. RMSPE results for NCA and nmc

See Tables 4–7.

C.2. Summary of model configurations used

See Table 8.

Code availability

All models and experiments were implemented in TensorFlow [87]. Further details regarding the experimental setup and the source code to reproduce the experimental results are available in the following public git repository: https://github.com/NahuelCostaCortez/DTW-Li-ion-Diagnosis.

References

[1] G.E. Blomgren, The development and future of lithium ion batteries, J. Electrochem. Soc. 164 (1) (2016) A5019.

[2] M.R. Palacín, Understanding ageing in Li-ion batteries: A chemical issue, Chem. Soc. Rev. 47 (13) (2018) 4924–4933.

[3] X. Han, L. Lu, Y. Zheng, X. Feng, Z. Li, J. Li, M. Ouyang, A review on the key issues of the lithium ion battery degradation among the whole life cycle, ETransportation 1 (2019) 100005.

[4] T. Waldmann, B.-I. Hogg, M. Wohlfahrt-Mehrens, Li plating as unwanted side reaction in commercial Li-ion cells–A review, J. Power Sources 384 (2018) 107–124.

[5] X. Lin, K. Khosravinia, X. Hu, J. Li, W. Lu, Lithium plating mechanism, detection, and mitigation in lithium-ion batteries, Prog. Energy Combust. Sci. 87 (2021) 100953.

[6] M. Dubarry, G. Baure, D. Anseán, Perspective on state-of-health determination in lithium-ion batteries, J. Electrochem. Energy Convers. Storage 17 (4) (2020).

[7] S. Yang, C. Zhang, J. Jiang, W. Zhang, L. Zhang, Y. Wang, Review on state-of-health of lithium-ion batteries: Characterizations, estimations and applications, J. Cleaner Prod. 314 (2021) 128015.

[8] A. Barai, K. Uddin, M. Dubarry, L. Somerville, A. McGordon, P. Jennings, I. Bloom, A comparison of methodologies for the non-invasive characterisation of commercial Li-ion cells, Prog. Energy Combust. Sci. 72 (2019) 1–31.

[9] M. Dubarry, V. Svoboda, R. Hwu, B.Y. Liaw, Incremental capacity analysis and close-to-equilibrium OCV measurements to quantify capacity fade in commercial rechargeable lithium batteries, Electrochem. Solid-State Lett. 9 (10) (2006) A454.

[10] X. Hu, L. Xu, X. Lin, M. Pecht, Battery lifetime prognostics, Joule 4 (2) (2020) 310–346.

[11] H. Rauf, M. Khalid, N. Arshad, Machine learning in state of health and remaining useful life estimation: Theoretical and technological development in battery degradation modelling, Renew. Sustain. Energy Rev. 156 (2022) 111903.

[12] D.N. How, M. Hannan, M.H. Lipu, P.J. Ker, State of charge estimation for lithium-ion batteries using model-based and data-driven methods: A review, Ieee Access 7 (2019) 136116–136136.

[13] Q. Li, D. Li, K. Zhao, L. Wang, K. Wang, State of health estimation of lithium-ion battery based on improved ant lion optimization and support vector regression, J. Energy Storage 50 (2022) 104215.

[14] H. Sun, J. Sun, K. Zhao, L. Wang, K. Wang, Data-driven ICA-bi-LSTM-combined lithium battery SOH estimation, Math. Probl. Eng. 2022 (2022).

[15] Z. Cui, L. Wang, Q. Li, K. Wang, A comprehensive review on the state of charge estimation for lithium-ion battery based on neural network, Int. J. Energy Res. 46 (5) (2022) 5423–5440.

[16] T. Baji, Evolution of the GPU device widely used in AI and massive parallel processing, in: 2018 IEEE 2nd Electron Devices Technology and Manufacturing Conference, EDTM, IEEE, 2018, pp. 7–9.

[17] W.Z. Khan, E. Ahmed, S. Hakak, I. Yaqoob, A. Ahmed, Edge computing: A survey, Future Gener. Comput. Syst. 97 (2019) 219–235.

[18] A. Dogra, R.K. Jha, S. Jain, A survey on beyond 5G network with the advent of 6G: Architecture and emerging technologies, IEEE Access 9 (2020) 67512–67547.

[19] D. Li, S. Li, S. Zhang, J. Sun, L. Wang, K. Wang, Aging state prediction for supercapacitors based on heuristic Kalman filter optimization extreme learning machine, Energy 250 (2022) 123773.

[20] Y. Lu, Artificial intelligence: A survey on evolution, models, applications and future trends, J. Manag. Anal. 6 (1) (2019) 1–29.

[21] C. Zhang, Y. Lu, Study on artificial intelligence: The state of the art and future prospects, J. Ind. Inform. Integr. 23 (2021) 100224.

[22] X. Shu, S. Shen, J. Shen, Y. Zhang, G. Li, Z. Chen, Y. Liu, State of health prediction of lithium-ion batteries based on machine learning: Advances and perspectives, Iscience 24 (11) (2021) 103265.

[23] L. Zhang, J. Lin, B. Liu, Z. Zhang, X. Yan, M. Wei, A review on deep learning applications in prognostics and health management, Ieee Access 7 (2019) 162415–162438.

[24] X. Sui, S. He, S.B. Vilsen, J. Meng, R. Teodorescu, D.-I. Stroe, A review of non-probabilistic machine learning-based state of health estimation techniques for lithium-ion battery, Appl. Energy 300 (2021) 117346.

[25] T. Lombardo, M. Duquesnoy, H. El-Bouysidy, F. Årén, A. Gallo-Bueno, P.B. Jørgensen, A. Bhowmik, A. Demortière, E. Ayerbe, F. Alcaide, et al., Artificial intelligence applied to battery research: Hype or reality? Chem. Rev. (2021).

[26] F. Wang, A. Preininger, AI in health: State of the art, challenges, and future directions, Yearb. Med. Inform. 28 (01) (2019) 016–026.

[27] J. Jumper, R. Evans, A. Pritzel, T. Green, M. Figurnov, O. Ronneberger, K. Tunyasuvunakool, R. Bates, A. Žídek, A. Potapenko, et al., Highly accurate protein structure prediction with AlphaFold, Nature 596 (7873) (2021) 583–589.

[28] P. Isola, J.-Y. Zhu, T. Zhou, A.A. Efros, Image-to-image translation with conditional adversarial networks, in: Proceedings of the IEEE Conference on Computer Vision and Pattern Recognition, 2017, pp. 1125–1134.

[29] L. Ward, S. Babinec, E.J. Dufek, D.A. Howey, V. Viswanathan, M. Aykol, D.A. Beck, B. Blaiszik, B.-R. Chen, G. Crabtree, et al., Principles of the battery data genome, 2021, arXiv preprint arXiv:2109.07278.

[30] Y. Zhang, R. Xiong, H. He, M.G. Pecht, Long short-term memory recurrent neural network for remaining useful life prediction of lithium-ion batteries, IEEE Trans. Veh. Technol. 67 (7) (2018) 5695–5705.

[31] X. Li, L. Zhang, Z. Wang, P. Dong, Remaining useful life prediction for lithium-ion batteries based on a hybrid model combining the long short-term memory and elman neural networks, J. Energy Storage 21 (2019) 510–518.

[32] W. Zhang, X. Li, X. Li, Deep learning-based prognostic approach for lithium-ion batteries with adaptive time-series prediction and on-line validation, Measurement 164 (2020) 108052.

[33] Y. Fan, F. Xiao, C. Li, G. Yang, X. Tang, A novel deep learning framework for state of health estimation of lithium-ion battery, J. Energy Storage 32 (2020) 101741.

[34] K. Liu, Y. Shang, Q. Ouyang, W.D. Widanage, A data-driven approach with uncertainty quantification for predicting future capacities and remaining useful life of lithium-ion battery, IEEE Trans. Ind. Electron. 68 (4) (2020) 3170–3180.

[35] S. Li, C. Ju, J. Li, R. Fang, Z. Tao, B. Li, T. Zhang, State-of-charge estimation of lithium-ion batteries in the battery degradation process based on recurrent neural network, Energies 14 (2) (2021) 306.

[36] S. Cui, I. Joe, A dynamic spatial-temporal attention-based GRU model with healthy features for state-of-health estimation of lithium-ion batteries, IEEE Access 9 (2021) 27374–27388.

[37] P.M. Attia, A. Bills, F.B. Planella, P. Dechent, G. Dos Reis, M. Dubarry, P. Gasper, R. Gilchrist, S. Greenbank, D. Howey, et al., "Knees" in lithium-ion battery aging trajectories, J. Electrochem. Soc. 169 (6) (2022) 060517.

[38] D. Anseán, M. Dubarry, A. Devie, B. Liaw, V. García, J. Viera, M. González, Operando lithium plating quantification and early detection of a commercial LiFePO4 cell cycled under dynamic driving schedule, J. Power Sources 356 (2017) 36–46.

[39] G. Baure, M. Dubarry, Synthetic vs. real driving cycles: A comparison of electric vehicle battery degradation, Batteries 5 (2) (2019) 42.

[40] G. Dos Reis, C. Strange, M. Yadav, S. Li, Lithium-ion battery data and where to find it, Energy AI (2021) 100081.

[41] S. Wang, S. Jin, D. Bai, Y. Fan, H. Shi, C. Fernandez, A critical review of improved deep learning methods for the remaining useful life prediction of lithium-ion batteries, Energy Rep. 7 (2021) 5562–5574.

[42] V.D. Angelis, Battery archive, 2022, URL www.batteryarchive.org.

[43] M. Dubarry, D. Beck, Big data training data for artificial intelligence-based Li-ion diagnosis and prognosis, J. Power Sources 479 (2020) 228806.

[44] M. Dubarry, D. Beck, Analysis of synthetic voltage vs. Capacity datasets for big data Li-ion diagnosis and prognosis, Energies 14 (9) (2021) 2371.

[45] S. Kim, Z. Yi, B.-R. Chen, T.R. Tanim, E.J. Dufek, Rapid failure mode classification and quantification in batteries: A deep learning modeling framework, Energy Storage Mater. 45 (2022) 1002–1011.

[46] M. Dubarry, G. Baure, A. Devie, Durability and reliability of EV batteries under electric utility grid operations: Path dependence of battery degradation, J. Electrochem. Soc. 165 (5) (2018) A773.

[47] M. Dubarry, A. Devie, K. Stein, M. Tun, M. Matsuura, R. Rocheleau, Battery energy storage system battery durability and reliability under electric utility grid operations: Analysis of 3 years of real usage, J. Power Sources 338 (2017) 65–73.

[48] J. Vetter, P. Novák, M.R. Wagner, C. Veit, K.-C. Möller, J. Besenhard, M. Winter, M. Wohlfahrt-Mehrens, C. Vogler, A. Hammouche, Ageing mechanisms in lithium-ion batteries, J. Power Sources 147 (1–2) (2005) 269–281.

[49] C.R. Birkl, M.R. Roberts, E. McTurk, P.G. Bruce, D.A. Howey, Degradation diagnostics for lithium ion cells, J. Power Sources 341 (2017) 373–386.

[50] M. Dubarry, C. Truchot, B.Y. Liaw, Synthesize battery degradation modes via a diagnostic and prognostic model, J. Power Sources 219 (2012) 204–216.

[51] H.M. Dahn, A. Smith, J. Burns, D. Stevens, J. Dahn, User-friendly differential voltage analysis freeware for the analysis of degradation mechanisms in Li-ion batteries, J. Electrochem. Soc. 159 (9) (2012) A1405.

[52] A. Smith, H.M. Dahn, J. Burns, J. Dahn, Long-term low-rate cycling of LiCoO2/graphite Li-ion cells at 55 C, J. Electrochem. Soc. 159 (6) (2012) A705.

[53] M. Ecker, J.B. Gerschler, J. Vogel, S. Käbitz, F. Hust, P. Dechent, D.U. Sauer, Development of a lifetime prediction model for lithium-ion batteries based on extended accelerated aging test data, J. Power Sources 215 (2012) 248–257.

[54] A. Barai, K. Uddin, W. Widanalage, A. McGordon, P. Jennings, The effect of average cycling current on total energy of lithium-ion batteries for electric vehicles, J. Power Sources 303 (2016) 81–85.

[55] A. Smith, J. Burns, D. Xiong, J. Dahn, Interpreting high precision coulometry results on Li-ion cells, J. Electrochem. Soc. 158 (10) (2011) A1136.

[56] F. Yang, D. Wang, Y. Zhao, K.-L. Tsui, S.J. Bae, A study of the relationship between coulombic efficiency and capacity degradation of commercial lithium-ion batteries, Energy 145 (2018) 486–495.

[57] P. Iurilli, C. Brivio, V. Wood, On the use of electrochemical impedance spectroscopy to characterize and model the aging phenomena of lithium-ion batteries: A critical review, J. Power Sources 505 (2021) 229860.

[58] D. Li, L. Wang, C. Duan, Q. Li, K. Wang, Temperature prediction of lithium-ion batteries based on electrochemical impedance spectrum: A review, Int. J. Energy Res. (2022).

[59] G. Piłatowicz, A. Marongiu, J. Drillkens, P. Sinhuber, D.U. Sauer, A critical overview of definitions and determination techniques of the internal resistance using lithium-ion, lead-acid, nickel metal-hydride batteries and electrochemical double-layer capacitors as examples, J. Power Sources 296 (2015) 365–376.
[60] A. Barai, K. Uddin, W. Widanage, A. McGordon, P. Jennings, A study of the influence of measurement timescale on internal resistance characterisation methodologies for lithium-ion cells, Sci. Rep. 8 (1) (2018) 1–13.
[61] M. Dubarry, M. Berecibar, A. Devie, D. Anseán, N. Omar, I. Villarreal, State of health battery estimator enabling degradation diagnosis: Model and algorithm description, J. Power Sources 360 (2017) 59–69.
[62] M. Dubarry, A. Devie, Battery durability and reliability under electric utility grid operations: Representative usage aging and calendar aging, J. Energy Storage 18 (2018) 185–195.
[63] M. Dubarry, C. Pastor-Fernández, G. Baure, T.F. Yu, W.D. Widanage, J. Marco, Battery energy storage system modeling: Investigation of intrinsic cell-to-cell variations, J. Energy Storage 23 (2019) 19–28.
[64] D. Anseán, G. Baure, M. González, I. Cameán, A. García, M. Dubarry, Mechanistic investigation of silicon-graphite/LiNi0. 8Mn0. 1Co0. 1o2 commercial cells for non-intrusive diagnosis and prognosis, J. Power Sources 459 (2020) 227882.
[65] K.S. Mayilvahanan, K.J. Takeuchi, E.S. Takeuchi, A.C. Marschilok, A.C. West, Supervised learning of synthetic big data for Li-ion battery degradation diagnosis, Batteries Supercaps (2021).
[66] S. Lee, Y. Kim, Li-ion battery electrode health diagnostics using machine learning, in: 2020 American Control Conference, ACC, IEEE, 2020, pp. 1137–1142.
[67] P. Tormene, T. Giorgino, S. Quaglini, M. Stefanelli, Matching incomplete time series with dynamic time warping: An algorithm and an application to post-stroke rehabilitation, Artif. Intell. Med. 45 (1) (2009) 11–34.
[68] T. Górecki, M. Łuczak, Non-isometric transforms in time series classification using DTW, Knowl.-Based Syst. 61 (2014) 98–108.
[69] M. Shah, J. Grabocka, N. Schilling, M. Wistuba, L. Schmidt-Thieme, Learning DTW-shapelets for time-series classification, in: Proceedings of the 3rd IKDD Conference on Data Science, 2016, 2016, pp. 1–8.
[70] M. Shokoohi-Yekta, B. Hu, H. Jin, J. Wang, E. Keogh, Generalizing DTW to the multi-dimensional case requires an adaptive approach, Data Min. Knowl. Discov. 31 (1) (2017) 1–31.
[71] M. Cuturi, M. Blondel, Soft-DTW: A differentiable loss function for time-series, in: International Conference on Machine Learning, PMLR, 2017, pp. 894–903.
[72] N. Begum, L. Ulanova, J. Wang, E. Keogh, Accelerating dynamic time warping clustering with a novel admissible pruning strategy, in: Proceedings of the 21th ACM SIGKDD International Conference on Knowledge Discovery and Data Mining, 2015, pp. 49–58.
[73] L. Tao, C. Lu, A. Noktehdan, Similarity recognition of online data curves based on dynamic spatial time warping for the estimation of lithium-ion battery capacity, J. Power Sources 293 (2015) 751–759.
[74] Y. Liu, C. Zhang, J. Jiang, Y. Jiang, L. Zhang, W. Zhang, Capacity estimation of serial lithium-ion battery pack using dynamic time warping algorithm, IEEE Access 7 (2019) 174687–174698.
[75] P. Hu, G. Ma, Y. Zhang, C. Cheng, B. Zhou, Y. Yuan, State of health estimation for lithium-ion batteries with dynamic time warping and deep kernel learning model, in: 2020 European Control Conference, ECC, IEEE, 2020, pp. 602–607.
[76] S. Kim, N.H. Kim, J.-H. Choi, Prediction of remaining useful life by data augmentation technique based on dynamic time warping, Mech. Syst. Signal Process. 136 (2020) 106486.
[77] D. Beck, P. Dechent, M. Junker, D.U. Sauer, M. Dubarry, Inhomogeneities and cell-to-cell variations in lithium-ion batteries, a review, Energies 14 (11) (2021) 3276.
[78] P. Virtanen, R. Gommers, T.E. Oliphant, M. Haberland, T. Reddy, D. Cournapeau, E. Burovski, P. Peterson, W. Weckesser, J. Bright, S.J. van der Walt, M. Brett, J. Wilson, K.J. Millman, N. Mayorov, A.R.J. Nelson, E. Jones, R. Kern, E. Larson, C.J. Carey, İ. Polat, Y. Feng, E.W. Moore, J. VanderPlas, D. Laxalde, J. Perktold, R. Cimrman, I. Henriksen, E.A. Quintero, C.R. Harris, A.M. Archibald, A.H. Ribeiro, F. Pedregosa, P. van Mulbregt, SciPy 1.0 Contributors, SciPy 1.0: Fundamental algorithms for scientific computing in python, Nature Methods 17 (2020) 261–272, http://dx.doi.org/10.1038/s41592-019-0686-2.
[79] W. Meert, K. Hendrickx, T. Craenendonck, Wannesm/dtaidistance v2. 0.0, 2020, Zenodo.
[80] A. Krizhevsky, I. Sutskever, G.E. Hinton, Imagenet classification with deep convolutional neural networks, Adv. Neural Inf. Process. Syst. 25 (2012) 1097–1105.
[81] O. Ronneberger, P. Fischer, T. Brox, U-Net: Convolutional networks for biomedical image segmentation, in: International Conference on Medical Image Computing and Computer-Assisted Intervention, Springer, 2015, pp. 234–241.
[82] A. Dosovitskiy, L. Beyer, A. Kolesnikov, D. Weissenborn, X. Zhai, T. Unterthiner, M. Dehghani, M. Minderer, G. Heigold, S. Gelly, et al., An image is worth 16x16 words: Transformers for image recognition at scale, 2020, arXiv preprint arXiv:2010.11929.
[83] L. Biewald, Experiment tracking with weights and biases, 2020, URL https://www.wandb.com/, Software available from wandb.com.
[84] X. Ying, An overview of overfitting and its solutions, J. Phys.: Conf. Ser. 1168 (2019) 022022.
[85] F. Zhuang, Z. Qi, K. Duan, D. Xi, Y. Zhu, H. Zhu, H. Xiong, Q. He, A comprehensive survey on transfer learning, Proc. IEEE 109 (1) (2020) 43–76.
[86] D. Anseán, M. Dubarry, A. Devie, B. Liaw, V. García, J. Viera, M. González, Fast charging technique for high power LiFePO4 batteries: A mechanistic analysis of aging, J. Power Sources 321 (2016) 201–209.
[87] M. Abadi, A. Agarwal, P. Barham, E. Brevdo, Z. Chen, C. Citro, G.S. Corrado, A. Davis, J. Dean, M. Devin, S. Ghemawat, I. Goodfellow, A. Harp, G. Irving, M. Isard, Y. Jia, R. Jozefowicz, L. Kaiser, M. Kudlur, J. Levenberg, D. Mané, R. Monga, S. Moore, D. Murray, C. Olah, M. Schuster, J. Shlens, B. Steiner, I. Sutskever, K. Talwar, P. Tucker, V. Vanhoucke, V. Vasudevan, F. Viégas, O. Vinyals, P. Warden, M. Wattenberg, M. Wicke, Y. Yu, X. Zheng, TensorFlow: Large-scale machine learning on heterogeneous systems, 2015, URL https://www.tensorflow.org/, Software available from tensorflow.org.